Tuning the porosity of hard carbons elaborated from sucrose

L Raspado, Lucie Speyer, Mickaël Bolmont, Sébastien Cahen, S Fontana, Claire Hérold

Journal of Physics and Chemistry of Solids xxx (xxxx) 112013

Contents lists available at ScienceDirect

Journal of Physics and Chemistry of Solids

journal homepage: www.elsevier.com/locate/jpcs

Tuning the porosity of hard carbons elaborated from sucrose

L. Raspado, L. Speyer, M. Bolmont, S. Cahen*, S. Fontana, C. Hérold

Institut Jean Lamour – UMR 7198 CNRS-Université de Lorraine, Groupe Matériaux Carbonés, Campus ARTEM – 2 Allée André Guinier, B.P. 50840, F54011, Nancy Cedex, France

ARTICLE INFO

Keywords:
Na-ion battery
Hard carbons
Pressure effect
Textural properties adjustment
Sodium intercalation mechanism

ABSTRACT

Hard carbons are among the most promising anode materials for Na-ion batteries (NIB) and are extensively studied. Nevertheless, it is still necessary to decipher the electrochemical intercalation behavior of sodium which is still under debate in the literature. Here, we present an innovating approach for elaborating hard carbon from simple sucrose precursor. It consists in a low-temperature pyrolysis at 500 °C under controlled argon pressure, followed by low-temperature carbonization. Using complementary characterization techniques (XRD, Raman, TEM, gas adsorption, SAXS) and galvanostatic electrochemical measurements, we show that this elaboration route allows the possibility to control and modify the porosity of the hard carbons without any modification of the structure of the material. This work leads us to assign the low potential plateau to the development of quasi-metal clustering of sodium into narrow porosity developed tuned thanks to the pyrolysis under pressure.

1. Introduction

Thanks to the abundance and low-cost of sodium, Na-ion batteries (NIB) are extensively studied as it is considered as a complementary technology to lithium-ion batteries (LIB). Indeed, if NIB have a lower specific energy density than lithium-ion systems mostly because of the higher atomic mass of sodium and its higher redox potential, they are sustainable and exhibit some technical advantages versus LIB. A challenging issue for the emergence of NIB remains the development of suitable negative electrode materials. Graphite, the most current material employed for LIB with a theoretical specific capacity of 372 mAh.g^{-1} cannot be considered for Na-ion systems, since sodium intercalates very poorly between graphene layers with a specific capacity reaching 35 mAh.g^{-1} only [1]. Hard carbons are non-graphitizable carbons materials extensively studied as negative electrodes in NIB and constitute excellent candidates for the replacement of graphite. They can be prepared by simple pyrolysis of abundant and easily available precursors such as saccharides and biomass waste [2]. Hard carbons can be depicted as small and curved randomly arranged graphitic domains forming a microporous structure, that cannot form any graphitic material even at very high temperatures [3,4]. This structural picture is a part of the explanation for the interactions between sodium ions and hard carbons which fit well with hard carbon as anode for NIB technology. Nevertheless, the precise storage mechanisms are not perfectly clear.

Galvanostatic cycling experiments performed on hard carbon electrodes tested in half-cell versus metallic sodium can be described with two distinct regions: a slope above 0.1 V vs Na^+/Na, and a plateau region below 0.1 V vs Na^+/Na. There seems to be a consensus about the first storage phenomenon, *i.e.* adsorption of sodium ions on the various defects (heteroatoms, structural defects, carbon edges …) of hard carbons: it is attributed to the slope region of the galvanostatic cycling signal for higher voltage. These defects are reactive sites, and are easily accessible, which explains that sodium interacts with these sites at higher voltage [5–8]. Some authors report correlations between the slope capacity and these defects [6,9–11]. In addition, the large variety of possible defects in hard carbons, which are disordered materials, creates an energetic distribution for the adsorption phenomena. Then, adsorption occurs on a quite large voltage range, in accordance with a sloping potential [5,7]. Moreover, it is well-known that defects tend to disappear when the temperature of pyrolysis increases, and the decrease of the capacity associated to the slope region with higher temperatures is a general observation [7,9,10,12]. In fact, the controversy concerns two other sodium storage phenomena: intercalation between graphene layers into the small graphitic domains, and closed micropore-filling.

The most current technique for probing the intercalation is *ex-situ*, *in-situ* and *operando* X-ray diffraction: a shift of the (002) peak to a lower angle indicates the increase of the interplanar distance due to the sodiation mechanism. However, as pointed out by Zhang et al. [13], since hard carbons are disordered materials, diffraction peaks are broad and a shift is difficult to assess clearly. It may explain the controversial results reported by X-ray diffraction and Raman spectroscopy in different studies: some authors observe shift signals during the high voltage

* Corresponding author.
E-mail address: sebastien.cahen@univ-lorraine.fr (S. Cahen).

https://doi.org/10.1016/j.jpcs.2024.112013
Received 9 January 2024; Received in revised form 23 February 2024; Accepted 19 March 2024
0022-3697/

reduction (slope region [14–16]) others below 0.1 V (the plateau region [5,6,12]), and some of them do not detect any sodium intercalation [13,17]. In some studies, intercalation is associated to the adsorption on defects on the slope region. An ionic state is reported for sodium on the slope region by Na nuclear magnetic resonance and X-ray photoelectron spectroscopy, nevertheless this ionic feature is in accordance with both phenomena [6,7,18,19]. Intercalation can be assigned to the end of the slope since defects are more reactive versus sodium ions than interlayer domains [7,20], and can even continue on the plateau region for smaller interplanar distances [20].

Concerning the micropore-filling mechanism, the pore volume and specific surface area of hard carbons decrease when the temperature of treatment increases together with an increase in the plateau capacity, but some authors indicate that this correlation between the texture and the plateau capacity is not relevant [10,11,21]. However, in many publications, the porosity is probed by gas adsorption only. Nevertheless, hard carbons are known to develop closed pores when the temperature of pyrolysis increases [15,22], *i.e.* pores which are not accessible to gas molecules, so physisorption provides partial information. In fact, an increase in the pyrolysis temperature implies a decrease in the accessible porosity concurrently with a development of the closed porosity not easily evidenced as the total porosity globally decreases.

Small-Angle X-ray Scattering (SAXS) allows a study of the overall porosity of hard carbons [23], and authors using this more reliable technique report the pore-filling on the plateau region [14,15,24,25]. The study of the electronic state of sodium by Na NMR and XPS on the plateau region indicates that it is close to a metallic state, which is in accordance with a quasi-metal sodium clustering into pores [7,18,19,26,27]. Moreover, closed pores are the less accessible sites in hard carbons, and their filling occur mainly for low diffusion rates, as measured by Galvanostatic Intermittent Titration Technique (GITT) [8,20,28]. Electrochemical dilatometry measurements are also in accordance with a micropore-filling on the plateau region [29,30]. Interestingly, Ilic et al. report that for a commercial hard carbon, the plateau capacity is progressively decreased after ball-milling, *i. e.* after the conversion of closed pores into open pores [31]. Some authors indicate that the pore-filling on the plateau region can occur in association with sodium intercalation [20,25]. The plateau capacity increases with higher temperatures of treatment, but for very high temperatures, a small decrease is sometimes reported. It is attributed to the structural changes in hard carbons at high temperature, especially the decrease of the interplanar distance with graphitization that limits the intercalation of sodium ions and then the closed pores filling (also in accordance with a contribution of intercalation if it occurs on the plateau region) [7,11,29,32,33].

It appears that the closed microporosity seems to be especially important for the development of the low-voltage plateau capacity. In addition, during the first charge-discharge cycles, the decomposition of the electrolyte occurs with the formation of a passivation layer, called SEI (Solid Electrolyte Interphase). The SEI can prevent the solvent intercalation and helps to the electrode stability and cyclability, but its formation consumes sodium ions and then lead to an irreversible capacity as well as cell polarization and diffusivity [14,34–36]. The main common strategy to limit the SEI formation is a decrease in the specific surface area of hard carbons [37], possibly addressed by pyrolyzing at high temperature. Such a thermal treatment also allows the development of closed porosity. The best materials regarding their electrochemical performances are usually reported around 1400–1500 °C, a temperature range that is quite energy consuming.

In this paper, we propose an innovative technique for elaborating hard carbons with a controlled porosity, using pressurized pyrolysis. The use of pressure has already been proposed as a solution for controlling porosity. The precursor can be heated in an autoclave [38,39] or treated in hydrothermal conditions [40]. By hydrothermal carbonization, some authors report the preparation of carbon microspheres with smooth surfaces which limits the SEI formation [41,42], but the porosity of the materials, especially the closed one, is not precisely determined. During pyrolysis, heteroatoms are progressively eliminated from the precursors as gaseous species, and our study postulates that applying a pressure would limit and/or control the gas emission out of the material. Then, the surface of the particles would be modified because less developed by gases activation, and a higher proportion of micropores would be closed. This would allow to develop a consequent plateau capacity together with limiting the SEI formation, even at relatively low temperatures.

If the chemical doping of hard carbons can be a considered strategy [43–45], it is important to optimize the texture of the materials. In this aim, a lot of studies about the sodium storage mechanisms are based on the preparation of hard carbons with different pyrolysis temperatures, and their physico-chemical and electrochemical characterization. A variation of temperature simultaneously implies the modification of the chemical, structural and textural properties of hard carbons, which makes difficult to assess the relationships between the different sections of the charge/discharge curves and the interactions between sodium ions and the materials. This bottleneck is one of the reasons why the sodium storage mechanisms are still under debate. A pressure variation is expected to have a significant influence on the porous texture only, maintaining the chemical composition and degree of graphitic order almost unchanged. Their electrochemical behavior should make the understanding of sodium storage mechanisms easier.

In line with this, a novel and simple pressurization device which can be connected to classical tubular furnace has been developed in our group. Then, hard carbons are elaborated from sucrose, a simple, sustainable and abundant precursor, under different pressures from 1 bar (atmospheric pressure) to 7 bar. Sucrose has also been chosen regarding the fact that such a carbohydrate is a thermosetting precursor without any initial porosity. In order to exclusively study the impact of the pressure on the evolution of the pore structure, it consists in an interesting starting point. Hard carbons prepared are then characterized using multi-scale techniques, and their electrochemical behavior is evaluated by galvanostatic cycling.

2. Methods and materials

2.1. Materials preparation

Hard carbons are prepared from commercial sucrose. Sucrose is first introduced in a silica boat and dehydrated at 180 °C during 24 h in a muffle furnace. The resulting brown solid is then pyrolyzed under argon flow in a stainless-steel tubular horizontal furnace.

It is worth noting that the furnace is pressurized, but still flushed by constant gas flow. By this way, argon and decomposition gases such as CO or CO_2 are eliminated from the atmosphere of the furnace which avoids the activation of the elaborated hard carbons and an undesired increase in the specific surface area. As argon flushes the surface of the formed carbon material which decomposes by forming activation gases (CO, CO_2, H_2O), it is necessary to regulate precisely the flow in order to control the activation phenomenon. This control is realized using a ball flowmeter adjusted at a constant value during the whole process. Elsewhere, the reactor is paired with the aforementioned pressurization device developed in our team in order to control the pressure without modifying the argon flow during the whole process.

Pressure is applied during the pyrolysis at 500 °C during 2 h, with a heating rate of 5 °C.min^{-1}, with a range from 1 to 7 bar controlled with a manometer. This step helps improving the cross-linking degree of the material. The as-obtained black solid is then hand-grinded, and finally carbonized in the same furnace, but under atmospheric pressure, at 850 °C or 950 °C during 3 h with a heating rate of 5 °C.min^{-1}. This step aims to increase the carbon content of the material and is realized at atmospheric pressure as the rigid skeleton of the carbon material has

been formed previously. If the [850°C–950 °C] temperature range remains relatively low regarding classical elaboration process of hard carbons, it has been selected in order to minimize the environmental footprint of the process. During all steps, the outcoming C_xH_y gases formed upon thermal treatments are neutralized using a burner continuously. Samples are finally subjected to 20 min of mild ball milling, mandatory for further characterizations.

2.2. Materials characterization

Elementary analysis was performed on a Thermo Fisher Flashsmart, by a 1 mg sampling. For transmission electron microscopy (TEM) observations, samples are first dispersed in ethanol and deposited on a copper grid with a holey carbon film, then observed with a Jeol ARM 200F microscope operating at 200 kV. X-ray diffractograms are acquired using a Bruker D8 Advance diffractometer with a molybdenum anticathode ($\lambda_{K\alpha1}$ = 70.930 pm) with a 1 h accumulation repeated 12 times, on an angular range from 2° to 50° (2θ). Samples are placed in Lindemann glass capillaries (1.5 mm diameter) and rotated at 10 rpm. Raman spectroscopy is carried out with a Horiba Jobin-Yvon LabRAM HR800 spectrometer operating at λ = 633 nm, after dispersion of the samples in ethanol and deposition on a glass slide, and 5 acquisitions have been performed on each sample. Adsorption isotherms (N_2 77 K and CO_2 273 K) are collected using a Micromeritics ASAP 2020 device, after outgassing the samples at 400 °C during 12 h. The specific surface areas, pore volumes and pore size distributions are calculated using the 2D-NLDFT model. Helium pycnometry is performed on a manual Sievert apparatus adapted for density measurement, with samples thermostated at 25 °C and outgassed during 72 h. Values of density are calculated from an average of five experimental points, with the error determined by the standard deviation between these points. Small angle X-Ray scattering (SAXS) measurements are carried out on a SAXSPace instrument (Anton Paar), using line-collimation system at the SAXS facility in the "PhotoNS technical platform of the L2CM laboratory UMR7053". This instrument is attached to a ID 3003 laboratory X-Ray generator (General Electric) equipped with a sealed X-Ray tube (PANalytical, $\lambda_{Cu,\ K\alpha}$ = 154.2 pm) operating at 40 kV and 50 mA. The samples were introduced in a Lindemann glass capillary, with a diameter equal to 2.0 mm, subsequently sealed, before being placed at 25 °C, inside an evacuated sample chamber equipped with a temperature-controlled sample holder unit, and exposed to X-Ray beam for about 30 min. Scattering of X-Ray beam is recorded by a 1D detector (Mythen 2 with strip of 50 μm × 8 mm) placed at 317 mm distance from sample. Scattering intensities I(q) are provided as a function of the magnitude of the scattering vector q = (4π/λ) sin(θ), where 2θ is the total scattering angle. Thanks to a translucent beam stop allowing the measurement of an attenuated primary beam at q = 0, all measured intensities can be calibrated by normalizing the attenuated primary intensity. The data are collected in a q-range from 0.13 to 7.7 nm^{-1} and then corrected for the background scattering, from the empty capillary and for slit-smearing effects by a desmearing procedure, using Lake method. After correction, obtained intensities are scaled into absolute units using water as a reference material.

2.3. Electrochemical characterization

80 wt% hard carbon, 10 wt% carbon black (Timcal SuperP) and 10 wt% polyvinylidene fluoride (PVDF) are mixed in N-methylpyrrolidone (NMP) until obtaining a homogeneous slurry. The slurry is coated onto a battery grade aluminum collector (16 μm thick) using a doctor blade and dried overnight at 80 °C under an argon flux in a Büchi furnace. 2032 coin cells are assembled under nitrogen atmosphere using 1 M $NaPF_6$ in 1:1 mass ratio ethylene carbonate/dimethyl carbonate (EC/DMC) solvent as electrolyte, a sodium disk and two glass microfiber disks as separators. All electrochemical tests are carried out with a BioLogic BCS 810 cycling station. Cells have been analyzed by galvanostatic cycling with potential limitation between 0.01 and 2.75 V (vs Na^+/Na) (discharged then charged), with two cycles at C/20 followed by twenty-five cycles at C/10 rate.

3. Results and discussion

For this study, five experimental conditions were chosen: two samples carbonized at 850 °C from 1 to 3 bar, and three carbons carbonized at 950 °C from 1 to 7 bar. The resultant hard carbons are referred as x-y, where x is the pressure applied during the pre-treatment (in bar) and y the pyrolysis temperature (in °C).

3.1. Chemical and structural analysis

Elementary analyses have been performed for the five hard carbon samples of this study and are reported in Supplementary Materials (Table S1). The carbon content reaches 84 wt% for samples carbonized at 850 °C, and between 86 wt% for those heated at 950 °C. As expected, the carbon content slightly increases by raising the temperature of the thermal treatment. Nevertheless, for a constant temperature of 950 °C, elementary analyses reveal that the chemical composition of hard carbons remains almost constant when increasing the pyrolysis pressure from 1 to 7 bar, in agreement with initial assumption.

To depict the structure of the five hard carbon samples, complementary techniques were used: X-Ray diffraction (XRD), Raman spectroscopy and TEM.

Structural characterizations were first performed by XRD measurements. Fig. 1 shows the corresponding powder XRD patterns revealing broad diffraction peaks which can be indexed as 002, 10*l*, 004 and 11*l* Bragg reflections. These patterns are typical of poor graphitized carbon materials with a 002 reflection at 10.20° and two smaller broad bands assigned to *hk*0 and *hkl* reflections. The presence of several superimposed peaks forming a broad contribution at 20° does not allow determining the lateral size of the crystallites (L_a value) by XRD. On the contrary, the reticular distance of the 002 reflection has been evaluated for each sample. From the Full-Width at Half-Maximum of the 002 Bragg peak (β^{mes}), the crystallite size along the **c**-axis noted L_c is calculated by using the Scherrer equation:

$$L_c = \frac{0.91.\lambda}{\cos\left(\theta_{002}\right).\beta_{mes}}$$

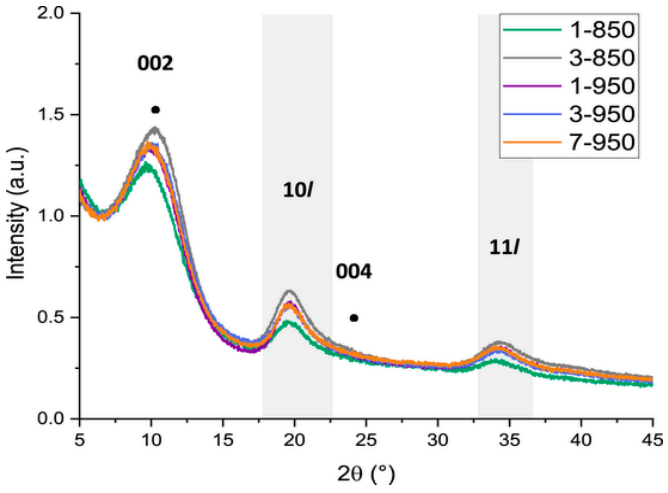

Fig. 1. Normalized powder XRD patterns of hard carbon samples ($\lambda_{Mo\ K\alpha1}$ = 70.930 pm).

As shown in Table 1, the results are quite similar regardless of the sample treatment. Indeed, whatever the temperature and the applied pressure, the data do not reveal any significative evolution of the sample structure.

If L_a cannot be evaluated from XRD data, Raman spectroscopy is a powerful tool for the structural characterization of low-graphitized carbon materials. Fig. 2 shows the nice overlapping of the Raman spectra for all samples and Fig. 3 illustrates the spectrum decomposition for the 7–950 sample with the adjusted functions for each individual contribution. Each spectrum presents two visible bands: the D band around 1350 cm^{-1} and the G band at 1580 cm^{-1}. Those bands respectively correspond to the breathing mode of benzenic cycles and to the tangential vibration mode in the carbon planes [43]. So, the intensity of the D band is directly proportional to the quantity of aromatic rings in the structure. Within the group of disordered carbons, the increase in I_D value indicates an ordering of the material due to a clustering of these cycles starting from an amorphous carbon to hard or glassy carbons. Note that it is the opposite tendency for graphitizable carbons, for which the development of the D band is correlated to the number of defects in the sp^2 carbon planes [46]. In the case of hard carbons, the presence of structural defects induces a peak enlargement, and I_D/I_G ratio remains interesting in order to highlight a possible evolution of ordering between hard carbons (corresponding values are reported in Table 1). A little variation between spectra is noted, as each sample shows an I_D/I_G ratio around 2.5 in agreement with this type of disordered materials. A quantitative analysis of the bands position, intensity and Full Width at Half Maximum (FWHM) is also available in Table S2.

However, other contributions appear necessary to fully model one spectrum as showed in Fig. 3. S and A bands represent other contributions due to disorder in the material, respectively associated to the respiration mode of benzene rings adjacent to heteroatoms, and the vibrational mode of sp^2 carbon atoms adjacent to defects, causing out-of-plane deformations [47]. The width of these bands and their intensities agree with a large amount of structural and chemical defects. In addition, the very weak signal at 2700 cm^{-1}, at the position of the 2D band dedicated for the stacking order along the **c**-axis, confirms there is no graphitization for this kind of carbon material.

Table 1
Summarized structural characterization of hard carbon samples from XRD and Raman spectroscopy analyses.

Sample	$2\theta_{002}$ (°Mo)	d_{002} (nm)	β^{mes}_{002} (°)	L_{002} (nm)	I_D/I_G	L_a (nm)
1–850	10.11	0.40	3.50	1.06	2.6	3.87
3–850	10.46	0.39	3.90	0.95	2.4	4.11
1–950	10.26	0.40	3.72	1.00	2.5	4.02
3–950	10.38	0.39	3.80	0.98	2.5	3.94
7–950	10.18	0.40	3.68	1.01	2.5	4.02

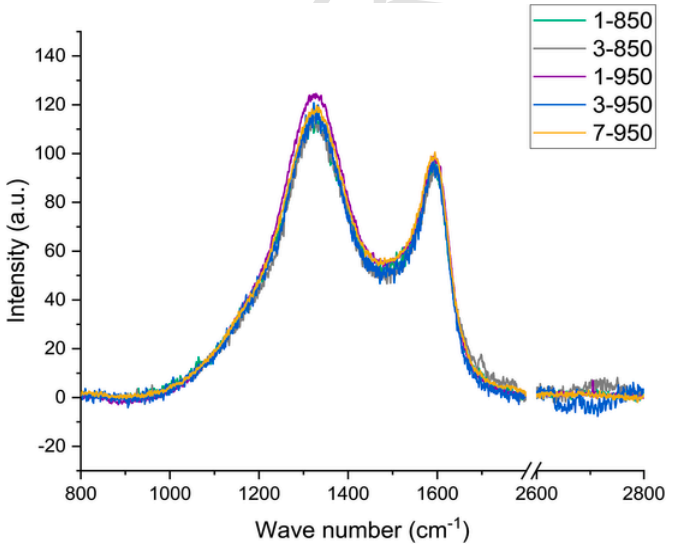

Fig. 2. Raman spectra (λ = 632.81 nm) of hard carbon samples, normalized on the G band (1593-1596 cm^{-1}).

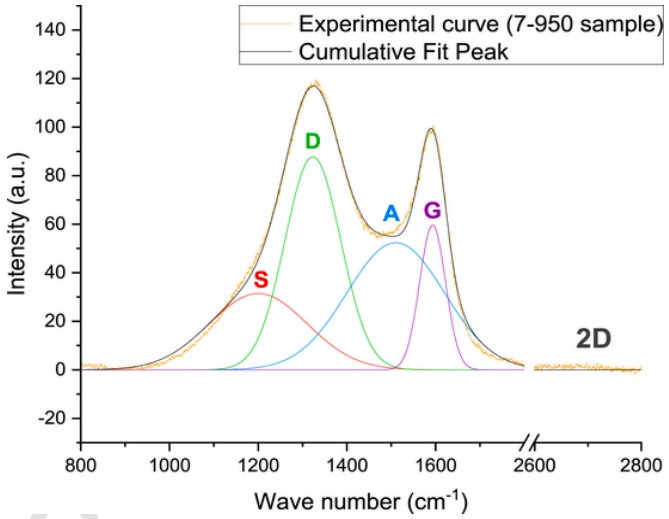

Fig. 3. Raman spectrum of 7–950 sample and its decomposition in S, D, A, G contributions according to Gauss functions.

According to the adaptation by Mallet-Ladeira et al. [48] of the Tuinstra and Koenig's law for carbon materials, the crystallite size in the (ab) plane, L_a value, can be estimated as follows:

$$L_a\,(nm) = \frac{4.4}{\frac{I_D}{I_G}} * \left(\frac{2.41}{E_L\,(eV)}\right)^4, with \quad E_L = \frac{h * C}{\lambda} = 1.9632\ eV$$

In Table 1, L_a values are all very close to 4 nm and confirm, according to the identical spectra shapes, that there are no notable structural differences between those materials.

Using X-ray diffraction and Raman spectroscopy, it appears that for the two studied temperatures, the pressure variation does not induce any significant modification of the structure of the materials. It remains however relevant to monitor the microstructure of the HC samples at the local scale by HRTEM experiments.

Fig. 4 shows TEM images of the different samples. As expected, micrographs reveal disordered structures with small aromatic domains and a low degree of graphitic order. However, it is locally possible to observe a slight structural evolution of the samples, due to the applied pressure and the carbonization temperature. Indeed, a statistical study between samples 1–850 and 7–950 has been performed. These samples have been selected in order to highlight any tiny local structural evolution with pressure and temperature. The comparison reveals a slight increase in the lateral size of the ordered domains as well as a local decrease in the interlayer distance from 0.43 nm to 0.38 nm, nevertheless in agreement with the average values calculated from diffractograms. The global appearance of the 7–950 sample reveals a less disordered structure with larger ordered domains. Although XRD and Raman spectroscopy observations show no modification of the structure by the pressure, TEM gives a relevant local trend indicating a possible local evolution in the microstructure of the samples.

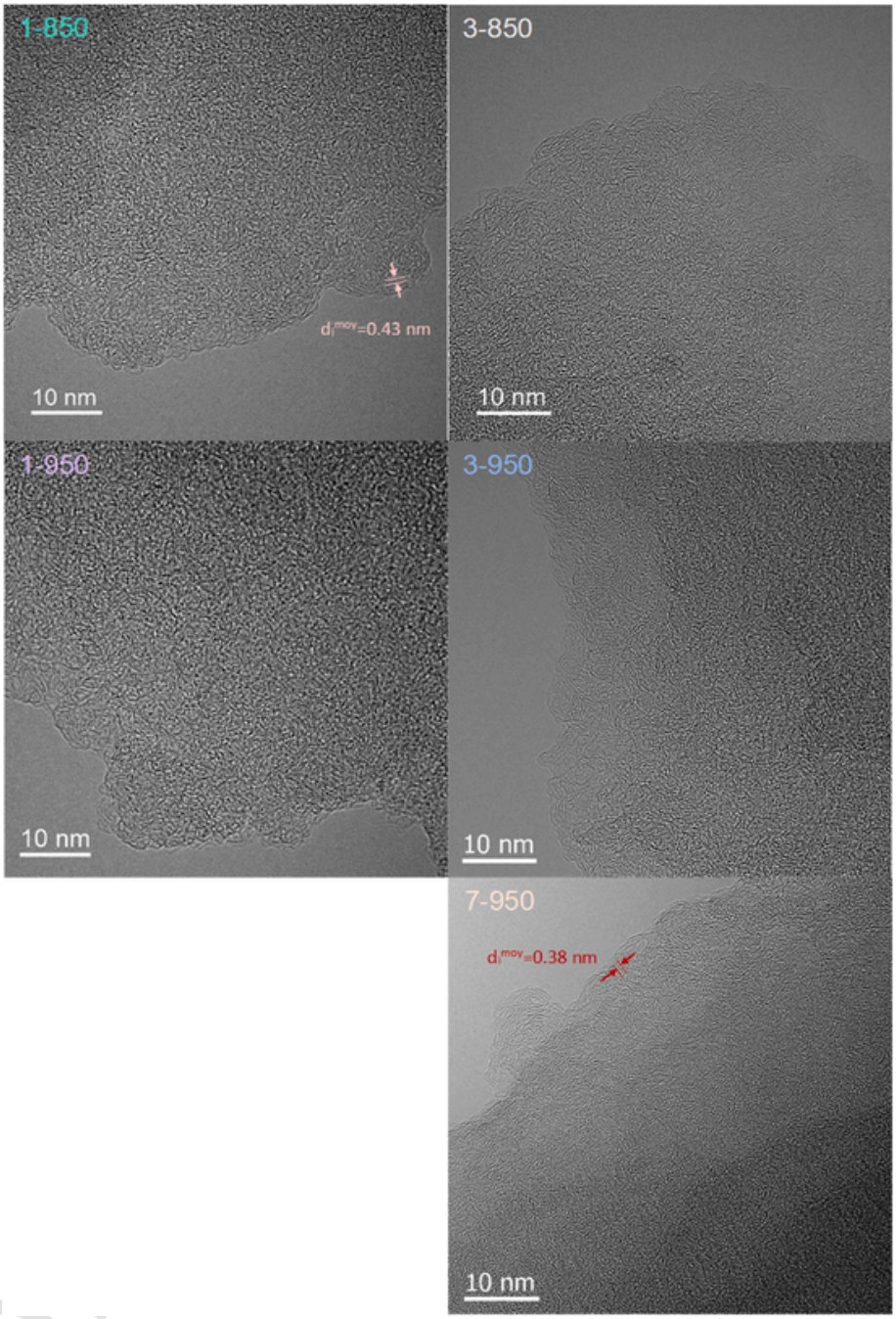

Fig. 4. TEM images of hard carbon samples.

3.2. Textural analysis

Determining the textural properties of hard carbon samples is essential to probe the effect of the pressure. As a first approach, adsorption volumetry is used to obtain information on the accessible porosity using two gas probe molecules. By N_2 adsorption at 77 K, each sample depicts a hybrid type-I isotherm with a vertical asymptote at low P/P_0 (corresponding to a microporous material) and type-II with an increase in adsorbed gas at higher P/P_0 representative for non-porous surfaces (Fig. 5). It appears also a hysteresis loop which is not closed for all the isotherms, assuming that the gases have difficulties to desorb the material due to the expected tortuosity of the pores in hard carbons. Differences are also notable between samples with the variation in the quantity of adsorbed nitrogen, linked with the amount of accessible porosity.

CO_2 adsorption at 273 K has also been investigated as a complementary gas probe molecule to characterize the ultramicroporosity of the material (< 0.7 nm). The corresponding isotherms are available in Fig. S1. 2D-NLDFT calculations have been performed to quantify the specific surface area (SSA) and the pore volumes available for each molecule, which values are reported in Table 2. Both values of N_2 and CO_2 adsorption are presented in Table 2 because of their complementarity.

Focusing on N_2 adsorption results for the 850 °C series, the values are quite high and present no significative change. Looking at the samples pyrolyzed at higher temperature, a trend appears with a significa-

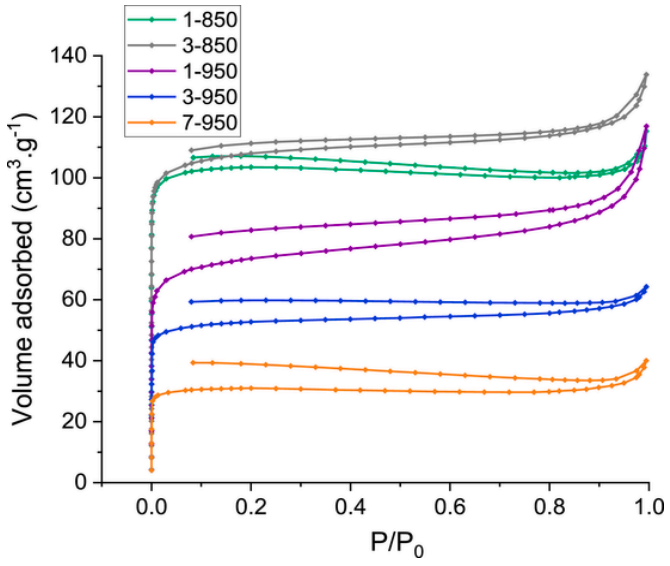

Fig. 5. Adsorption isotherms (N_2 at 77 K) of hard carbon samples.

Table 2
Specific surface areas and pore volumes calculated by 2D-NLDFT model from N_2 and CO_2 adsorption isotherms, and average density measured by helium pycnometry.

Sample	SSA_{DFT} N_2 ($m^2.g^{-1}$)	Micropore volume N_2 ($cm^3.g^{-1}$)	Ultramicropore volume CO_2 ($cm^3.g^{-1}$)	He density
1–850	549	0.164	0.181	1.86
3–850	564	0.197	0.168	1.82
1–950	316	0.161	0.170	2.00
3–950	209	0.092	0.162	1.85
7–950	127	0.055	0.159	1.88

tive decrease of SSA and pore volume with a threefold factor between 1 and 7 bar, in agreement with a significant influence of the pressure at this temperature. Moreover, a huge difference of pore volume is evidenced comparing the two gas probe molecules, with systematically higher values for the CO_2 contribution. It means that hard carbons contain a non-negligible quantity of ultramicropores. Regarding on CO_2 results, ultramicropore volume seems to follow the same trend, with a slower and homogeneous decrease whether for the 850 °C or 950 °C series. Even at 7 bar, a large amount of ultramicropores remains, which are hard to close even with pressure.

To improve the textural analysis of the HC depending on the probe molecule, pore size distributions determined by N_2 or CO_2 adsorption have been extracted from 2D-NLDFT calculations and plotted on Fig. 6. Figures (a) and (b) show a main distribution peak centered at 0.9 nm (for N_2 adsorption the peaks under 0.7 nm being not relevant because nitrogen adsorption is not reliable to characterize ultra-microporosity) whose intensity decreases between 850 and 950 series, well matching with a decrease in N_2 pore volume when rising the carbonization temperature (see Table 2). A shift toward smaller pore size appears for 3–850 and even more clearly for 7–950, which confirms that the pressure shrinks the size of accessible micropores. For ultramicropores, size distributions are better evaluated by CO_2 adsorption (Fig. 6c and d), and there is no significant change between 850 and 950 °C series in terms of pore diameters, showing mainly sizes centered at 0.4 and 0.6 nm. Nevertheless, the same shift seen with N_2 distribution is also observed with higher pressurized samples, but only for the 0.6 nm peak. So, the effect of the applied pressure tends to lightly decrease the pore size even for ultramicropores, along with the creation of larger pores still only accessible by CO_2 as showed by the appearance of a broad peak above 0.8 nm for both temperatures.

Density values given in Table 2 have been measured by helium pycnometry, and are a key to understand the evolution of closed porosity which is not characterized by gas adsorption. Indeed, for a single temperature, the density decreases when the applied pressure increases, which is an indicator of the creation of porosity inaccessible for helium molecules as well as other gas probe molecules (N_2 et CO_2).

SAXS is also a determinant analysis technique probing the whole microporosity, open and closed one, which is complementary to gas adsorption [23]. Fig. 7 shows SAXS curves fitted using a classical model for hard carbons [22,31,49–51]:

$$I(q) = \frac{A}{q^4} + \frac{B.a_1^4}{\left(1 + q^2.a_1^2\right)^2} + D$$

The first term corresponds to the small q values and the diffusion of macropores (*i.e.* the surface of particles), and A is proportional to the surface area of macropores. The second term represents the diffusion of micropores: B is proportional to the surface area of micropores and a_1 is proportional to their gyration radius. D is a background term. From B and a_1 values, a volume V proportional to the pore volume can be estimated [31]:

$$V = B.a_1$$

Since V_{SAXS} is proportional to total pore volume, a scaling factor (the same for all samples) is applied to V in order to estimate SAXS volumes (V_{SAXS}) which are comparable to pore volumes obtained from adsorption (N_2 and CO_2) measurements. a_1, B, V and V_{SAXS} values are listed in Table S3.

Fig. 8 shows the comparison of V_{SAXS} and pore volumes V_{N2} and V_{CO2} given by adsorption results, as a function of pressure and for each temperature of carbonization.

At 850 °C, the difference between SAXS and adsorption pore volumes is not significant for both gases, but becomes higher at 950 °C. As SAXS simultaneously detects open and closed pores, this increasing difference is attributed to a development of micropores which are inaccessible to N_2 [2–5]. The progressive micropore closure when the thermal treatment temperature increases is a well-known phenomenon [22]. At 950 °C, one can notice that the difference between pore volume determined by SAXS and gas adsorption increases with pressure in the case of N_2, and decreases in the case of CO_2. It can be confirmed by an estimation of the closed pore (CP) volume, given by the difference between V_{SAXS} and V_{N2}, and the proportion of closed pore volume %CP:

$$CP = V_{SAXS} - V_{N2}$$

$$\%CP = \frac{V_{SAXS} - V_{N2}}{V_{SAXS}} \times 100$$

The comparison between CP and %CP calculated for both gases would not be appropriated because SAXS does not discriminate ultramicropores from micropores. It is worth noting that V_{SAXS} is proportional to the total micropore volume (open and closed). Then, it should be clarified that CP and %CP are only estimated values (although the scaling factor between V and V_{SAXS} is adjusted so that CP values present the same order of magnitude as values reported in the literature [20,28,52]. The CP and %CP variations are plotted as a function of pressure on Fig. 9.

The increase in CP and %CP calculated from N_2 adsorption measurements indicates that pressure generates a progressive closure of pores which are accessible to this probe molecule. In fact, it is known that the reticulation of carbohydrates happens at relatively low temperature below 500–600 °C [53,54]. So, applying a mechanical force at this temperature upon pyrolysis will induce a direct impact on the pore formation, such as the collapse of the porosity which is formed by gas genera-

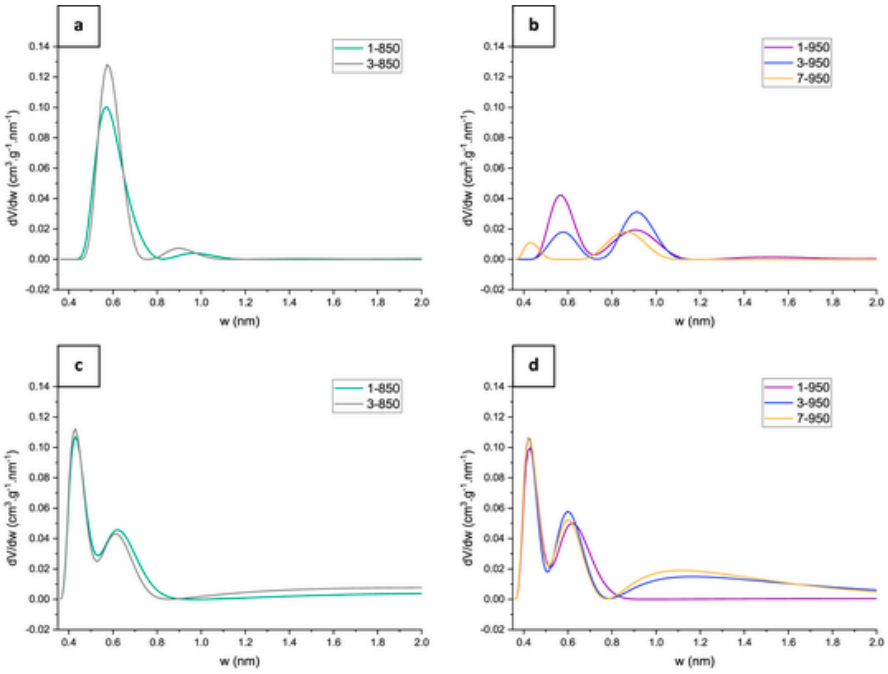

Fig. 6. Pore size distribution calculated by 2D-NLDFT on N_2 adsorption isotherms of 850 °C series (a) and 950 °C series (b), and on CO_2 adsorption isotherms of 850 °C series (c) and 950 °C series (d).

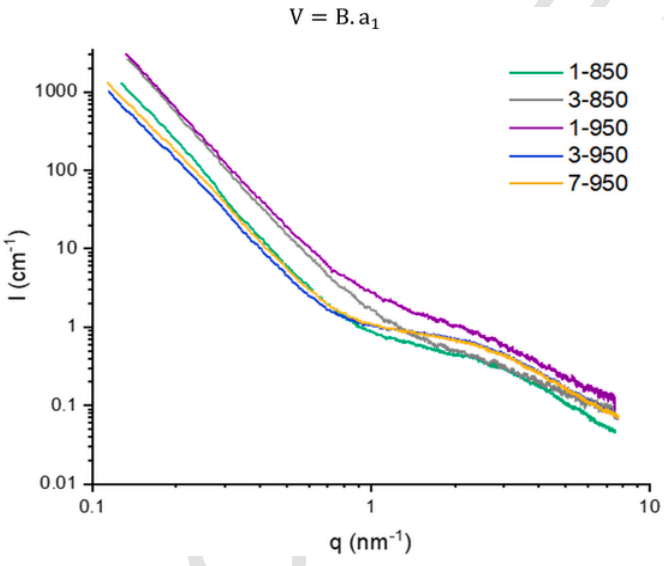

Fig. 7. SAXS curves for hard carbon samples.

tion (as illustrated by an experimental weight loss of 60% after this step). This porosity evolution is revealed by the evolution of the shape of the SAXS curves. As mentioned earlier, it is not possible to conclude concerning the ultramicropore closure: as the ultramicropore volume remains almost constant, we postulate that applying a pressure during the pyrolysis step closes the largest micropores, which is sufficient to decrease the overall density of the samples.

3.3. Electrochemical characterizations

In order to probe the role of the ultramicroporosity on the electrochemical sodiation, hard carbons carbonized at 950 °C series have been integrated into coin cells face to metallic sodium in order to perform galvanostatic cycling. Several tests have been realized and representative results are presented. Due to the very low influence of pressure on the textural properties of 850° samples, only electrochemical characterizations of 950° series are presented. Fig. 10 shows the resultant discharge and charge curves at C/20 current rate then followed by cycles at C/10.

As expected, the galvanostatic curves show a shape with the two well defined region of a typical NIB hard carbon anode: a high potential decreasing as a slope, then a low-voltage plateau. Little differences appear between the three samples and especially the 7–950, which show a better stability between each cycle, reflecting a better cycling behavior. In order to fully describe the curves, initial coulombic efficiency (ICE) and reversible capacities have been reported in Table 3 for the three samples, considering two regions: the slope, covering the range between 2.75 and 0.1 V, and the plateau in the 0.1–0.01 V range.

The increase in pressure during hard carbon elaboration induces several phenomena. For the first cycle, the value of ICE seems to increase slightly which is relevant considering the decreasing in specific surface observed by N_2 adsorption for these materials. The less accessible surface to the electrolyte is developed, the less a SEI layer can be formed leading to a decrease in the irreversible capacity.

For a single cycle, the value of total capacity seems to be globally equivalent between samples, resulting by a decrease in the slope capacity together with an increase in the plateau capacity. In the literature, the slope region is generally dedicated to defects and intercalation into graphitic domains, but also to capacitive adsorption on the surface at higher potentials. So, it should be noted that simultaneously with the decrease of the N_2 specific surface area we can note a shortening of this slope at higher pressure. Nevertheless, there are too many contributions on this wide range of potential to interpret its evolution in a clear and meaningfully way.

For the plateau part, its higher length for 7–950 sample well highlights that more created closed porosity (as supported by textural analysis) can be sodiated. This is relevant with an increase in the sodium clustering phenomenon [52]. This correlation makes us possible to as-

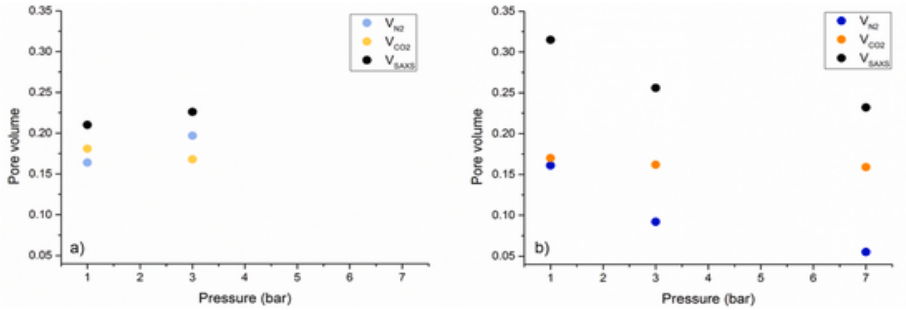

Fig. 8. Comparison of pore volumes calculated from adsorption and estimated by from SAXS at a) 850 °C b) 950 °C.

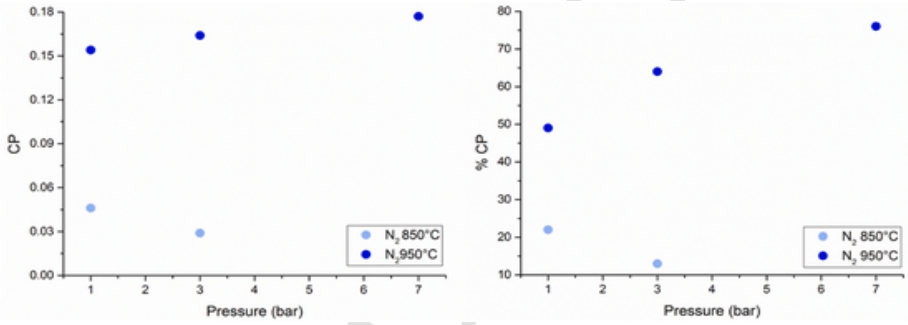

Fig. 9. Estimation of closed pore volume CP and proportion of closed pore volume %CP.

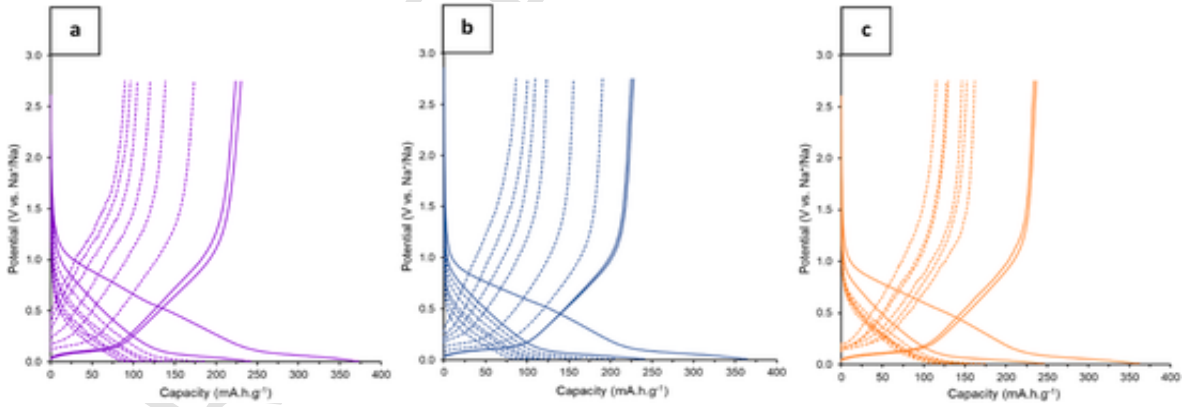

Fig. 10. Galvanostatic cycling curves of 1–950 (a), 3–950 (b) and 7–950 (c). Samples were cycled at C/20 twice (full lines) then at C/10 25 times (dashed lines, only the 1st, 5th,10th, 15th, 20th and 25th cycles are showed at C/10).

Table 3
Data retrieved from galvanostatic measurement for the 950 °C series at their 2nd cycle at C/20.

Sample	ICE (%)	Total reversible capacity (mA.h.g^{-1})	Slope capacity (mA.h.g^{-1})	Plateau capacity (mA.h.g^{-1})	Slope proportion (%)	Plateau proportion (%)
1–950	61.8	242.1	137.1	105.0	56.6	43.4
3–950	62.6	240.9	120.1	120.8	49.9	50.1
7–950	65.4	245.9	120.7	125.2	49.1	50.9

sign the Na^+ filling of closed porosity with the low potential plateau on galvanostatic curve, as also proposed by other authors [55,56].

The same quantitative analysis has been realized on several charge/discharge cycles and the results are given in Fig. 11.

A tendency seems to appear with the 7–950 sample which slope and plateau capacities tend to quickly fall and then stabilize between cycle 5 and 10 to reach the higher values of capacities afterward. It is also important to notice the different behavior between the two regions. On Fig. 11a, the gap of capacity between each sample on a single cycle is reduced compared to the values of plateau capacity more scattered (Fig. 11b). The little variations of slope capacity, especially at the last cycles, could be correlated with the subtle differences at the very local scale presented by TEM. The plateau was expected to vary more with the pressure, as depict on Fig. 11b with bigger differences at each cycle. As

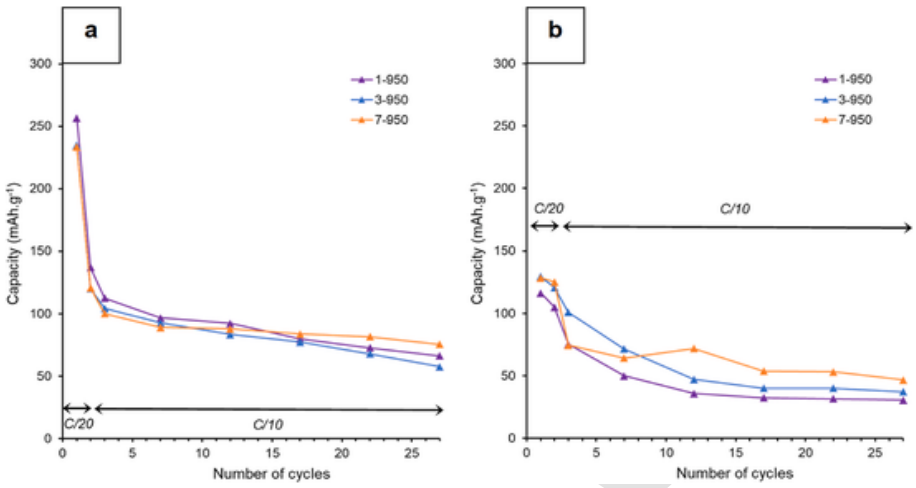

Fig. 11. Evolution of slope (a) and plateau (b) capacities depending of different cycles for 950 °C hard carbon samples.

demonstrated with SAXS results, 7–950 contain a higher amount of closed porosity and is expected to maximize clustering during cycling at low potential. It's indeed the case regarding on Fig. 11b, where 7–950 have the higher plateau potential on almost all cycles. This other evidence supports the assumption of a quasi-metal clustering in developed closed porosity.

In order to get a better picture of the global performances of the different hard carbons, total values of reversible capacities of all cycles are reported on Fig. 12. The same tendencies are observed, especially for 7–950 which capacity decreases faster at the first cycles, then reaches the highest capacities after stabilization. The differences between 1-950 and 3–950 samples are smaller after the 10th cycle, so a high pressure is mandatory to fully highlight an influence in terms of capacity. This is the same conclusion with the cycling behavior, with 7–950 which appears to be more stable on this cycling time. Regarding the difference between the 3rd and the 27th cycle (corresponding to the 1st and last cycle at C/10), we obtain 91, 110 and 52 mAh.g^{-1} respectively for 1–950, 3–950 and 7–950. So, the high-pressure sample seems to be the optimal hard carbon on this range of pressure for electrochemistry applications.

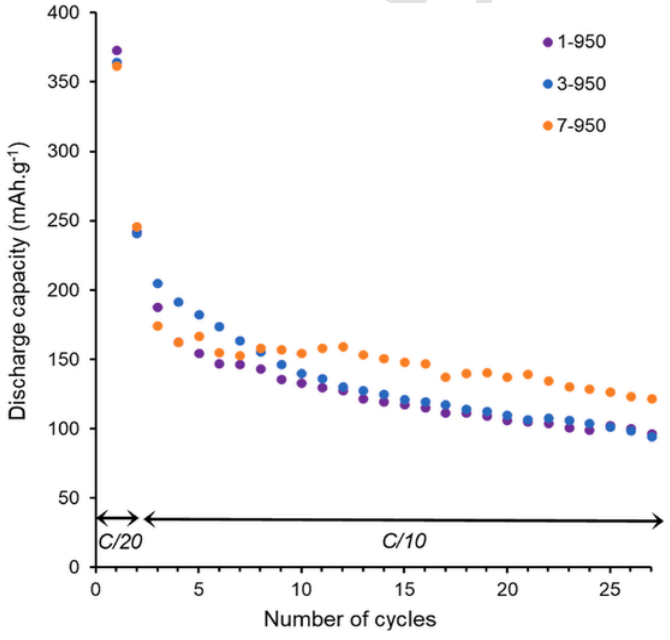

Fig. 12. Evolution of discharge capacities for cycles at C/20 and C/10.

Divergences are less obvious in terms of coulombic efficiency (CE), whose values are plotted in Fig. S2. Excepted for the 1st and 2nd cycle at C/20, each hard carbon tends to stabilize with a CE above 90%, and remaining almost stable during the 25 cycles, proving that pressure has not a significant influence on the capacity fade.

4. Conclusion

In this paper, preparation of hard carbons has been performed from simple sucrose precursor. A new way of hard carbon elaboration is presented which specificity is a pyrolysis step under argon pressure. Elemental analysis, XRD, Raman spectroscopy and TEM measurements allow to affirm that the chemical composition and the structure are not affected by the applied pressure during the pyrolysis treatment. Conversely, the porosity is clearly modified at high pressure, and even at moderate temperatures, a pressure of a few bars allows a micropore closure and then a clear decrease in the specific surface area and N_2 pore volume. The pressure variation makes it possible to study of the evolution of the textural properties exclusively, what cannot be envisaged if chemical or structural properties are modified by modifying the carbonization temperature. The combination of N_2 and CO_2 gas adsorption, SAXS, and helium pycnometry revealed an increase in closed porosity inside of the studied materials.

This study also aims to address the electrochemical insertion of Na^+ ions into hard carbons, under debate in the literature. In this work, looking at the galvanostatic cycling experiments, we assume that the low potential plateau is well correlated with the increase of closed porosity, that makes it possible the attribution of this low potential region to sodium sorption phenomena supposed as near-metal clustering of sodium ions inside of internal pores. This result constitutes an interesting step concerning the study of sodium sorption phenomena in hard carbons. Finally, comparing the electrochemical performances of several hard carbons, it seems that the sample pyrolyzed at 7 bar is an optimal material among the studied pressure range.

Funding sources

This work has been possible thanks to the financial support of ICEEL Carnot in frame of the EBNaR project.

CRediT authorship contribution statement

L. Raspado: Writing – review & editing, Writing – original draft, Visualization, Investigation, Formal analysis. **L. Speyer:** Writing – review & editing, Writing – original draft, Visualization, Validation, Supervision, Methodology, Investigation, Formal analysis. **M. Bolmont:** Writing – review & editing, Investigation, Formal analysis. **S. Cahen:** Writing – review & editing, Writing – original draft, Visualization, Validation, Supervision, Resources, Project administration, Methodology, Formal analysis, Conceptualization. **S. Fontana:** Writing – review & editing, Visualization, Validation, Supervision, Methodology, Investigation, Funding acquisition, Formal analysis. **C. Hérold:** Writing – review & editing, Writing – original draft, Visualization, Validation, Supervision, Resources, Project administration, Methodology, Funding acquisition, Formal analysis, Conceptualization.

Declaration of competing interest

The authors declare that they have no known competing financial interests or personal relationships that could have appeared to influence the work reported in this paper.

Data availability

No data was used for the research described in the article.

Acknowledgments

First, the authors want to thank Jean-François MARECHE for fruitful discussions concerning carbon science and his huge knowledge concerning the carbon-materials elaboration. He and Thierry SCHWEITZER are also acknowledged for their technical support. We also thank Mélanie EMO from CC 3 M for TEM experiments, Ghouti MEDJAHDI from CC Xgamma for his support in XRD measurements and Sébastien HUPONT for his contribution to Raman spectroscopy experiments. The authors greatly acknowledge the Plateforme PhotoNS of the L2CM Laboratory, University of Lorraine, for the SAXS analysis and Sandrine Adach from SynBioN for elemental analysis (UMR 7053 CNRS-UL; http://synbion.univ-lorraine.fr/accueil/).

Appendix A. Supplementary data

Supplementary data to this article can be found online at https://doi.org/10.1016/j.jpcs.2024.112013.

References

[1] P. Ge, M. Fouletier, Electrochemical insertion of sodium in graphite, Solid State Ionics 28 (1988) 1172, https://doi.org/10.1016/0167-2738(88)90351-7.
[2] D. Saurel, B. Orayech, B. Xiao, et al., From charge storage mechanism to performance : a roadmap toward high specific energy sodium-ion batteries through carbon anode optimization, Adv. Energy Mater. 8 (2018) 1703268, https://doi.org/10.1002/aenm.201703268.
[3] P.J.F. Harris, Structure of non graphitising carbons, Int. Mater. Rev. 42 (1997) 206–218, https://doi.org/10.1179/imr.1997.42.5.206.
[4] F.G. Emmerich, Evolution with heat treatment of crystallinity in carbons, Carbon 12 (1995) 1709–1715, https://doi.org/10.1016/0008-6223(95)00127-8.
[5] C. Bommier, T.W. Surta, M. Dolgos, et al., New mechanistic insights in Na-ion storage in nongraphitizable carbon, Nano Lett. 15 (2015) 5888, https://doi.org/10.1021/acs.nanolett.5b01969.
[6] S. Alvin, H. Cahyadi, J. Hwang, et al., Revealing the intercalation mechanisms of lithium, sodium, and potassium in hard carbons, Adv. Energy Mate. 10 (2020) 2000283, https://doi.org/10.1002/aenm.202000283.
[7] H. Au, H. Alptekin, A. Jensen, et al., A revised mechanistic model for sodium insertion in hard carbons, Energy Environ. Sci. 13 (2020) 3469, https://doi.org/10.1039/D0EE01363C.
[8] X. Zhang, W. Chen, J. Peng, et al., Pore structure modification of pitch-derived hard carbon for enhanced pore filling sodium storage, Energy Technol. 10 (2022) 2200612, https://doi.org/10.1002/ente.202200612.
[9] S. Qiu, L. Xiao, M.L. Sushko, et al., Manipulating adsorption-insertion mechanisms in nanostructured carbon materials for high efficiency sodium ion storage, Adv. Energy Mater. 7 (2017) 1700403, https://doi.org/10.1002/aenm.201700403.
[10] C. Ghimbeu, J. Gorka, V. Simone, et al., Insights on the Na+ ion storage mechanism in hard carbon: discrimination between the porosity, surface functional groups and defects, Nano Energy 44 (2018) 327, https://doi.org/10.1016/j.nanoen.2017.12.013.
[11] A. Gomez-Martin, J. Martinez-Fernandez, M. Ruttert, et al., Correlation of structure and performance of hard carbons as anodes for sodium-ion batteries, Chem. Mater. 31 (2019) 7288, https://doi.org/10.1021/acs.chemmater.9b01768.
[12] J. Ding, H. Wang, Z. Li, et al., Carbon nanosheet frameworks derived from peat moss as high performance sodium-ion battery anodes, ACS Nano 7 (2013) 11004, https://doi.org/10.1021/nn404640c.
[13] B. Zhang, C.M. Ghimbeu, C. Laberty, et al., Correlation between microstructure and Na storage behavior in hard carbon, Adv. Energy Mater. 6 (2016) 1501588, https://doi.org/10.1002/aenm.201501588.
[14] S. Komaba, W. Murata, T. Ishikawa, et al., Electrochemical Na insertion and solid electrolyte interphase for hard-carbon electrodes and applications to Na-ion batteries, Adv. Funct. Mater. 21 (2011) 3859, https://doi.org/10.1002/adfm.201100854.
[15] D.A. Stevens, J.R. Dahn, The mechanisms of lithium and sodium insertion in carbon materials, J. Electrochem. Soc. 148 (2001) 803–811, https://doi.org/10.1149/1.1379565.
[16] J.S. Weaving, A. Lim, J. Millichamp, et al., Elucidating the sodiation mechanism in hard carbon by operando Raman spectroscopy, ACS Appl. Energy Mater. 3 (2020) 7474, https://doi.org/10.1021/acsaem.0c00867.
[17] P. Bai, Y. He, X. Zou, et al., Elucidation of the sodium storage mechanism in hard carbons, Adv. Energy Mater. 8 (2018) 1703217, https://doi.org/10.1002/aenm.201703217.
[18] Z. Yu, et al., Hard carbon micro-nano tubes derived from kapok fibers as anode materials for sodium-ion batteries and the sodium storage mechanism, ChemComm (2020), https://doi.org/10.1039/C9CC08221B.
[19] Y. Li, Y. Hu, M. Titirici, et al., Hard carbon microtubes made from renewable cotton as high performance anode material for sodium-ion batteries, Adv. Energy Mater. 6 (2016) 1600659, https://doi.org/10.1002/aenm.201600659.
[20] X. Chen, et al., An overall understanding of sodium storage behaviors in hard carbons by an « adsorption-intercalation/filling » hybrid mechanism, Adv. Energy Mater. (2022), https://doi.org/10.1002/aenm.202200886.
[21] H. Lu, F. Ai, Y. Jia, et al., Exploring sodium-ion storage mechanism in hard carbons with different microstructure prepared by ball-milling method, Small 14 (2018) 1802694, https://doi.org/10.1002/smll.201802694.
[22] E.R. Buiel, A.E. George, J.R. Dahn, Model of micropore closure in hard carbon prepared from sucrose, Carbon 37 (1999) 1399, https://doi.org/10.1016/S0008-6223(98)00335-2.
[23] D. Saurel, J. Segalini, M. Jauregui, et al., A SAXS outlook on disordered carbon materials for electrochemical energy storage, Energy Storage Mater. 21 (2019) 162, https://doi.org/10.1016/j.ensm.2019.05.007.
[24] Y. Morikawa, S. Nishimura, R. Hashimoto, et al., Mechanism of sodium storage in hard carbon: a X-ray scattering analysis, Adv. Energy Mater. 10 (2020) 1903176, https://doi.org/10.1002/aenm.201903176.
[25] B. Tratnik, et al., Correlating structural properties with electrochemical behavior of non-graphitizable carbons in Na-ion batteries, ACS Appl. Energy Mater. (2022), https://doi.org/10.1021/acsaem.2c01390.
[26] K. Gotoh, T. Ishikawa, S. Shimadzu, et al., NMR study for electrochemically inserted Na in hard carbon electrode of sodium ion battery, J. Power Sources 225 (2013) 137, https://doi.org/10.1016/j.jpowsour.2012.10.025.
[27] J.M. Stratford, P.K. Allan, O. Pecher, et al., Mechanistic insights into sodium storage in hard carbon anodes using local structure probes, Chem. Commun. 52 (2016) 12430, https://doi.org/10.1039/C6CC06990H.
[28] S. Zhou, Z. Tang, Z. Pan, et al., Regulating closed pore structure enables significantly improved sodium storage for hard carbon pyrolyzing at relatively low temperature, SusMat 2 (2022) 357, https://doi.org/10.1002/sus2.60.
[29] H. Alptekin, et al., Sodium storage mechanism investigations through structural changes in hard carbons, ACS Appl. Energy Mater. (2020), https://doi.org/10.1021/acsaem.0c01614.
[30] I. Escher, et al., In situ (operando) electrochemical dilatometry as a method to distinguish charge storage mechanisms and metal plating processes for sodium and lithium ion sin hard carbon battery electrodes, Adv. Mater. Interfaces (2022), https://doi.org/10.1002/admi.202100596.
[31] I.K. Ilic, K. Schutjajew, W. Zhang, et al., Changes of porosity of hard carbons during mechanical treatment and the relevance for sodium-ion anodes, Carbon 186 (2022) 5, https://doi.org/10.1016/j.carbon.2021.09.063.
[32] S. Alvin, et al., Revealing sodium ion storage mechanism in hard carbon, Carbon (2019), https://doi.org/10.1016/j.carbon.2018.12.112.
[33] N. Sun, et al., Extended adsorption-insertion model: a new insight into the sodium storage mechanism of hard carbons, Adv. Energy Mater. 9 (2019) 1901351, https://doi.org/10.1002/aenm.201901351.
[34] Q. Zhang, J. Pan, P. Lu, et al., Synergetic effects of inorganic components in solid electrolyte interphase on high cycle efficiency of lithium ion batteries, Nano Lett. 16 (2016) 2011, https://doi.org/10.1021/acs.nanolett.5b05283.
[35] H. Kumar, E. Detsi, D. Abraham, et al., Fundamental mechanisms of solvent decomposition involved in solid-electrolyte interphase formation in sodium ion batteries, Chem. Mater. 28 (2016) 8930, https://doi.org/10.1021/acs.chemmater.6b03403.
[36] C. Bommier, D. Leonard, Z. Jian, et al., New paradigms on the nature of solid electrolyte interphase formation and capacity fading of hard carbon anodes in Na-ion batteries, Adv. Mater. Interfaces 3 (2016) 1600449, https://doi.org/10.1002/

admi.201600449.
[37] C. Bommier, W. Luo, W. Gao, et al., Predicting capacity of hard carbon anodes in sodium-ion batteries using porosity measurements, Carbon 76 (2014) 165, https://doi.org/10.1016/j.carbon.2014.04.064.
[38] Y. Han, C. Dabin, K. Nakabayashi, et al., Effect of heat pre-treatment conditions on the electrochemical properties of mangrove wood-derived hard carbon as an effective anode material for lithium-ion batteries, Electrochim. Acta 213 (2016) 432, https://doi.org/10.1016/j.electacta.2016.07.138.
[39] K. Nakabayashi, C. Dabin, Y. Han, et al., Structural effects on the enhancement of first-cycle Coulombic efficiency of mangrove-derived hard carbon as an anode material in sodium ion batteries, SN Appl. Sci. 1 (2019) 177, https://doi.org/10.1007/s42452-018-0141-5.
[40] S.A. Nicolae, H. Au, P. Modugno, et al., Recent advances in hydrothermal carbonization: from tailored carbon materials and biochemicals to applications and bioenergy, Green Chem. 22 (2020) 4747, https://doi.org/10.1039/D0GC00998A.
[41] V. Pol, E. Lee, D. Zhou, et al., Spherical carbon as a new high-rate anode for sodium-ion batteries, Electrochim. Acta 127 (2014) 61, https://doi.org/10.1016/j.electacta.2014.01.132.
[42] Z. Jian, Z. Xing, C. Bommier, et al., Hard carbon microspheres: potassium-ion anode versus sodium-ion anode, Adv. Energy Mater. 6 (2016) 1501784, https://doi.org/10.1002/aenm.201501874.
[43] F. Xie, et al., Hard carbons for sodium-ion batteries and beyond, Prog. Energy 2 (2020) 042002, https://doi.org/10.1088/2516-1083/aba5f5.
[44] S. Wu, H. Peng, J. Xu, et al., Nitrogen/phosphorus co-doped ultramicropores hard carbon spheres for rapid sodium storage, Carbon 218 (2024) 118756, https://doi.org/10.1016/j.carbon.2023.118756.
[45] S. Wu, H. Peng, L. Huang, et al., P-doped hard carbon microspheres for sodium-ion battery anodes with superior rate and cyclic performance, Inorg. Chem. Front. 10 (2023) 5908–5916, https://doi.org/10.1039/D3QI01296D.
[46] A.C. Ferrari, J. Robertson, Interpretation of Raman spectra of disordered and amorphous carbon, Phys. Rev. B 61 (2000) 14095, https://doi.org/10.1103/PhysRevB.61.14095.
[47] M.W. Smith, I. Dallmeyer, T.J. Johnson, et al., Structural analysis of char by Raman spectroscopy: improving band assignments through computational calculations from first principles, Carbon 100 (2016) 678–692, https://doi.org/10.1016/j.carbon.2016.01.031.
[48] P. Mallet-Ladeira, P. Puech, C. Toulouse, et al., A Raman study to obtain crystallite size of carbon materials: a better alternative to the Tuinstra–Koenig law, Carbon 80 (2014) 629–639, https://doi.org/10.1016/j.carbon.2014.09.006.
[49] M. Kalliat, C.Y. Kwak, P.W. Schmidt, Small-angle X-ray investigation of the porosity in coals, New Approach. Coal Chem. (1981) 3–22, https://doi.org/10.1021/bk-1981-0169.ch001.
[50] M. Dahbi, M. Kiso, K. Kubota, et al., Synthesis of hard carbon from argan shells for Na-ion batteries, J. Mater. Chem. A 5 (2017) 9917–9928, https://doi.org/10.1039/C7TA01394A.
[51] F. Xie, Z. Xu, A.C.S. Jensen, et al., Hard-soft carbon composite anodes with synergistic sodium storage performance, Adv. Funct. Mater. 29 (2019) 1901072, https://doi.org/10.1002/adfm.201901072.
[52] Y. Li, Y. Lu, Q. Meng, et al., Regulating pore structure of hierarchical porous waste cork-derived hard carbon anode for enhanced Na storage performance, Adv. Energy Mater. 9 (2019) 1902852, https://doi.org/10.1002/aenm.201902852.
[53] J.J. Kipling, J.N. Sherwood, P.V. Shooter, et al., Factors influencing the graphitization of polymer carbons, Carbon 1 (1964) 315–318, https://doi.org/10.1016/0008-6223(64)90285-4.
[54] J.S. McDonald-Wharry, M. Manley-Harris, et al., Reviewing, combining, and updating the models for the nanostructure of non-graphitizing carbons produced from oxygen-containing precursors, Energy Fuels 30 (2016) 7811–7826, https://doi.org/10.1021/acs.energyfuels.6b00917.
[55] H. Tonnoir, D. Huo, C. Davoisne, et al., Pyrolysis temperature dependence of sodium storage mechanism in non-graphitizing carbons, Carbon 208 (2023) 216–226, https://doi.org/10.1016/j.carbon.2023.03.055.
[56] X. Feng, Y. Li, et al., Unlocking the local structure of hard carbon to grasp sodium-ion diffusion behavior for advanced sodium-ion batteries, Energy Environ. Sci. 17 (2024) 1387–1396, https://doi.org/10.1039/D3EE03347C.